

# High Aspect Ratio Electrospun CuO Nanofibers as Anode Material for Lithium-Ion Batteries with Superior Cycleability

Rahul Sahay,<sup>†,‡,||</sup> Palaniswamy Suresh Kumar,<sup>†,‡,||</sup> Vanchiappan Aravindan,<sup>§,||</sup> Jayaraman Sundaramurthy,<sup>†,‡</sup> Wong Chui Ling,<sup>§</sup> Subodh G. Mhaisalkar,<sup>†,§</sup> Seeram Ramakrishna,<sup>‡,⊥,\*</sup> and Srinivasan Madhavi<sup>†,§,\*</sup>

<sup>†</sup>School of Materials Science and Engineering, Nanyang Technological University, 50 Nanyang Avenue, Singapore 639798

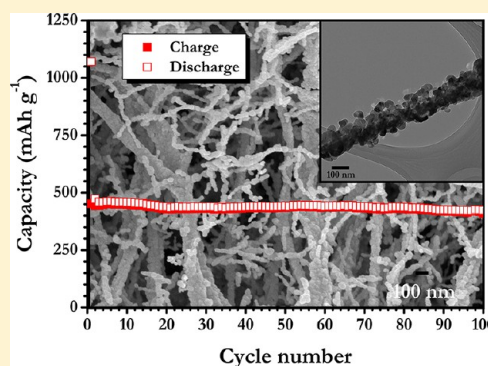
<sup>‡</sup>NUS Nanoscience and Nanotechnology Initiative, National University of Singapore, Singapore 117576

<sup>§</sup>Energy Research Institute @ NTU (ERI@N), Nanyang Technological University, Research Techno Plaza, 50 Nanyang Drive, Singapore 637553, Singapore

<sup>⊥</sup>Center for Nanofibers and Nanotechnology, National University of Singapore, Singapore 117576

## Supporting Information

**ABSTRACT:** A simple and efficient sol–gel/electrospinning technique is employed for the preparation of high aspect ratio CuO nanofibers. Characterizations studies including X-ray diffraction, scanning electron microscopy, High-resolution-transmission electron microscopy are employed to analyze the crystal structure, and morphology of electrospun CuO nanofibers. Electrochemical lithium storage properties are evaluated in half-cell configurations at room temperature between 0.005 and 3 V vs Li. Cyclic voltammetry is used to study the reaction mechanism during charge–discharge process. Electrospun CuO nanofibers delivered stable reversible capacity of 452 mAh g<sup>−1</sup> at current density of 100 mA g<sup>−1</sup> in half-cell configuration (Li/CuO nanofibers). The cell displayed the very stable cycling behavior up to 100 cycles at current density of 100 mA g<sup>−1</sup>. Rate capability studies of CuO nanofibers are conducted and presented. Our studies have shown that the enhanced cycleability of CuO electrospun nanofibers are due to the fibrous morphology formed by nanoscopic CuO particles which could not only increase the electrode/electrolyte contact area but also enables the facile partial reduction of Cu<sub>2</sub>O into metallic particles (Cu<sup>0</sup>).



## INTRODUCTION

In the last 2 decades, nanoarchitectures of materials ranging from metals to metal oxides and their composite have been explored for energy storage devices such as batteries and supercapacitors<sup>1–4</sup> on virtue of their unique properties such as high specific surface area, shorter ion diffusion, and electrochemical activity. Nanostructured materials bring unique advantages as electrode materials in lithium ion batteries (LIB) such as shorter lithium diffusion pathways, larger electrode/electrolyte contact area, facile lithium insertion/extraction as compared to their conventional bulk counterparts.<sup>5,6</sup> Various methods have been employed for the synthesis of nanostructured materials, including chemical vapor deposition,<sup>7</sup> hydrothermal,<sup>8</sup> sol–gel,<sup>9</sup> electrochemical deposition,<sup>10</sup> and electrospinning.<sup>11–14</sup> Nevertheless, research is ongoing on a reliable and economic process for the production of large-scale, high-quality one-dimensional nanoarchitectures such as nanofibers,<sup>11–14</sup> nanorods,<sup>15</sup> nanowire,<sup>16</sup> nanotubes,<sup>17</sup> etc. Among them, electrospinning is one of the efficient techniques to pattern the materials in nanometric ranges with size geometry that provides highly crystalline, high surface area,

and porous interconnected nanostructured materials with high yield.<sup>11</sup>

Since the commercialization of LIBs by Sony in 1990, carbonaceous anodes have dominated in practical LIBs that are used for portable and mobile applications.<sup>18</sup> Electric vehicles (EV) and hybrid electric vehicles (HEV) require high capacity anode materials than commercially available graphitic anodes (theoretical capacity ~372 mAh g<sup>−1</sup>).<sup>19</sup> Thus, several alternate insertion hosts were proposed for the place of graphite, unfortunately those materials exhibiting lower capacity and higher lithium insertion potentials than graphitic anodes.<sup>4</sup> Hence, search for high capacity anode materials are warranted and research focus is directed toward their utilization of transition metal oxides (TMO) as possible negative electrodes for LIBs. Generally, nanosized transition metal oxides undergo conversion reaction with lithium according to the following equilibrium proposed by Poizot et al.,<sup>20</sup>  $M_xO_y + 2yLi^+ + 2ye^- \leftrightarrow xM^0 + yLi_2O$ , where M belongs to transition metals such as

Received: June 1, 2012

Revised: July 26, 2012

Published: August 3, 2012

Fe, Co, Ni, Cu, etc. According to the above reaction, during first discharge, structural destruction takes place to remove oxygen from TMO to form amorphous  $\text{Li}_2\text{O}$  matrix in which ultrafine nanosized particulates of transition element in metallic state ( $\text{M}^0$ ) has been embedded. Owing to the multiple electron reaction, the obtained reversible capacity ( $>400 \text{ mAh g}^{-1}$ ) for nanosized transition metal oxides are well over graphitic anodes. As a result, several transition metal oxides with various morphologies have been explored as possible negative electrode material for LIB applications.<sup>21</sup>

Among the transition metal oxides, CuO is noteworthy to explore as possible anode material for LIB applications, due to its low-cost, ease of synthesis and eco-friendliness.<sup>22</sup> CuO is also a very important *p*-type semiconductor with a band gap of 1.2 eV and extensively studied in various applications such as catalysts,<sup>23</sup> gas sensors,<sup>24</sup> photoconductive/photochemical cells, and other electronic devices.<sup>25</sup> Nevertheless, few reports are also available on electrochemical lithium storage properties of CuO nanostructures either in native or composite form. Chen et al.<sup>26</sup> reported electrochemical performance of CuO polycrystalline nanowires prepared by wet-chemical method and exhibited higher reversible capacity than theoretical capacity ( $720$  and  $650 \text{ mAh g}^{-1}$  for 1 and 100 cycles, respectively at  $0.05 \text{ C}$  rate) but with irregular cycling behavior. Synthesis of CuO nanodisc/multiwalled carbon nanotube composites (MWCNT) through dehydrogenation of one-dimensional  $\text{Cu}(\text{OH})_2$  nanowires at  $60^\circ\text{C}$  was studied by Seo et al.<sup>27</sup> and delivered reversible capacities of  $657$  and  $440 \text{ mAh g}^{-1}$  for first and 20th cycles at  $0.2 \text{ C}$  rate with severe capacity fading. Dandelion-like hollow microspheres of CuO were reported by Wang et al.<sup>28</sup> and experienced poor cycleability with higher reversible capacity of  $\sim 750 \text{ mAh g}^{-1}$  at  $0.2 \text{ C}$  rate. Huang et al.<sup>29</sup> reported the performance of CuO/C hollow spheres and experiencing capacity fade from  $560 \text{ mAh g}^{-1}$  (first cycle) to  $440 \text{ mAh g}^{-1}$  (50th cycle) at current density of  $100 \text{ mA g}^{-1}$ . The CuO with complex hollow structure was suggested by Ju and Ryu<sup>30</sup> and showing poor cycling behavior with reversible capacity of  $<400 \text{ mAh g}^{-1}$ . Hierarchical hollow micro/nanostructures of CuO via green way approach suggested by Gao et al.<sup>31</sup> and delivered the reversible capacities of  $\sim 560$  and  $\sim 300 \text{ mAh g}^{-1}$  for first and 20th cycles, respectively at  $0.1 \text{ C}$  rate. Pillow shaped CuO synthesized by Wan et al.<sup>32</sup> and delivered the reversible capacities of  $\sim 370$  and  $\sim 320 \text{ mAh g}^{-1}$  for first and 50th cycles at  $0.1 \text{ C}$  rate. Solution route synthesized CuO ultrafine nanowires showed reversible capacity of  $\sim 115 \text{ mAh g}^{-1}$  higher than the theoretical value with capacity fade during cycling reported by Wang et al.<sup>33</sup> Ke et al.<sup>34</sup> suggested nanoribbon like morphology of CuO and test cell delivered a reversible capacity of  $495 \text{ mAh g}^{-1}$  at current density of  $100 \text{ mA g}^{-1}$  showing an increasing trend of capacity profile. Those previous literature studies clearly illustrates that, capacity fading is the main issue for CuO while employing them as anode material for LIBs. Further, it was observed that the electrochemical performances of CuO were strongly influenced by the nature of synthesis and its morphology. Hence, an attempt has been made to improve the cycling stability of CuO, we have synthesized one-dimensional CuO nanofibers with interconnected particulates by electrospinning technique for first time. The electrochemical performances of CuO nanofibers (CuO–NF) were evaluated in half-cell configurations (Li/CuO–NF) and described in detail along with its physical properties.

## ■ EXPERIMENTAL SECTION

Analytical grade, copper acetate (99%), polyvinyl alcohol (PVA,  $M_w = 80\,000$  to  $124\,000$ ) were purchased from Aldrich and used as received without any further purification. First,  $0.5 \text{ g}$  of the copper acetate ( $\text{Cu}(\text{CH}_3\text{COO})_2 \cdot \text{H}_2\text{O}$ ) was dissolved in  $4.5 \text{ mL}$  of  $10 \text{ wt } \%$  aqueous PVA solution. This solution was continuously stirred for  $24 \text{ h}$  at room temperature conditions leading to the formation of pale blue colored copper hydroxide/PVA sol. The as-prepared sol was transferred to  $10 \text{ mL}$  syringe with a hypodermic needle (diameter  $27 \text{ G}$ ) in a controlled electrospinning setup (ELECTROSPUNRA, Singapore). The obtained optimal conditions for electrospun nanofibers were a flow rate of  $0.2 \text{ mL/h}$  and applied electric field of  $1.25 \text{ kV/cm}$ . The fiber mat was harvested and annealed at  $800^\circ\text{C}$  for  $12 \text{ h}$  to yield CuO nanofibers (CuO–NF). The heating and cooling ramp rate during sintering process were kept at  $2$  and  $5^\circ\text{C/min}$ , respectively.

Structural characterizations were conducted using Bruker AXS, D8 Advance X-ray diffractometer equipped with  $\text{Cu K}\alpha$  radiation. Rietveld crystal structure refinement was carried out using Topas V3 software. Morphological features and internal structure of CuO–NF were studied using field emission scanning electron microscope (FE-SEM, JEOL JSM-7600F) and transmission electron microscope (TEM, JEOL 2100F), respectively. Electrochemical characterizations were carried out using standard two-electrode coin-cell configuration (CR 2016) at room temperature. The composite electrodes were prepared by mixing  $10 \text{ mg}$  of active material (CuO–NF),  $1.5 \text{ mg}$  of super P, and  $1.5 \text{ mg}$  of binder (Teflonized acetylene black, TAB-2). The mixture was pressed on a  $200 \text{ mm}^2$  stainless steel mesh (thickness  $0.25 \text{ mm}$ , Goodfellow, UK) current collector and dried at  $60^\circ\text{C}$  for overnight before conducting cell assembly under Ar filled glovebox (MBraun, Germany). The electrodes were separated by microporous glass fiber separator (Whatman, Cat. No. 1825–047, UK) and  $1 \text{ M LiPF}_6$  in ethylene carbonate (EC)/diethyl carbonate (DEC) ( $1:1 \text{ wt } \%$ , DAN VEC) mixture was used as the electrolyte solution. Cyclic voltammetric (CV) traces were recorded using Solartron, 1470E and SI 1255B impedance/gain-phase analyzer coupled with a potentiostat in two electrode configuration, in which metallic lithium was used as both counter and reference electrodes. Galvanostatic cycling performances were recorded at constant current mode between  $0.005$  and  $3 \text{ V}$  vs Li at current density of  $100 \text{ mA g}^{-1}$  using an Arbin 2000 battery tester.

## ■ RESULTS AND DISCUSSION

Figure 1 represents the thermogravimetric-derivative thermal analysis (TGA/DTA) of as-spun fibers. Thermal studies were performed in a controlled atmosphere to measure the rate of weight loss of as-spun (CuO/PVA composite nanofiber) sample as a function of temperature. The observed traces were categorized in to three main thermal events: (i) The temperature range between  $30$  and  $100^\circ\text{C}$  is attributed to the loss of moisture as well as trapped solvent, i.e., water. The endothermic DTA peak around  $100^\circ\text{C}$  also confirms the evaporation of water. (ii) The temperature range from  $100$  to  $300^\circ\text{C}$  and this particular weight loss may be ascribed to the loss of bound water and decomposition of acetate group along with the degradation of PVA. The sharp exothermic DTA peaks around  $196$  and  $261^\circ\text{C}$  are consistent with the decomposition of acetate groups and polymer decomposition in as-spun CuO/PVA composite nanofiber. (iii) The temperature range  $300$ –

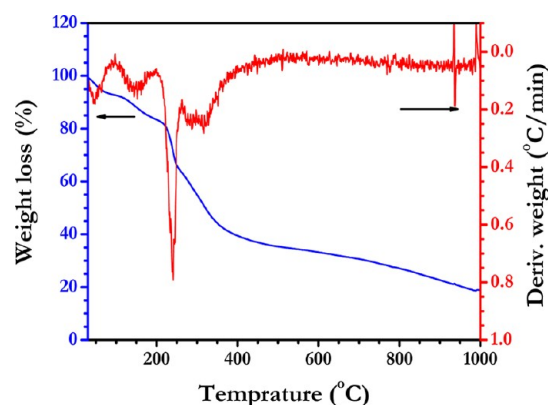


**Figure 1.** Thermogravimetric-derivative thermal analysis of as-spun CuO nanofibers recorded in the oxygen environment at the scan rate of 5 °C/min.

500 °C corresponds to the decomposition of the main PVA chain and subsequent removal of residual polymer aggregates.<sup>23</sup> Absence of exothermic DTA peaks from 500 to 1000 °C predicts no further thermal events occurred. This thermal study clearly suggests that, the synthesis temperature above 500 °C is required to yield high quality CuO nanofibers and the resultant fiber appeared black in color.

Rietveld refined powder X-ray diffraction pattern of sintered CuO–NF are illustrated in Figure 2. The observed reflections

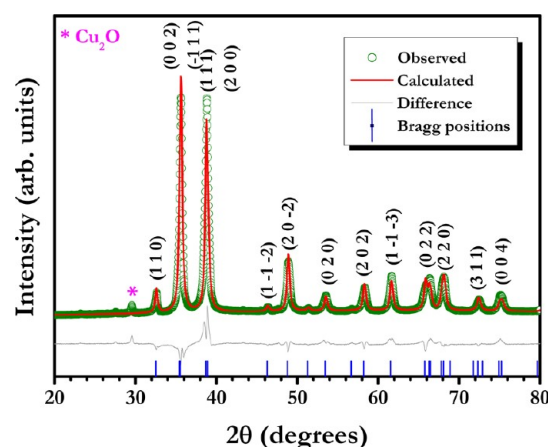


**Figure 2.** Rietveld refined X-ray diffraction pattern of electrospun CuO nanofibers.

were indexed according to the monoclinic structure with C2/c space group. The observed pattern clearly showed the satellite peaks, which is indicative of highly crystalline nature of sintered CuO–NF and PVA has been completely burned out during the calcination process as evident from TGA-studies. The observed reflections contained trace amount of Cu<sub>2</sub>O as impurity phase. Lattice parameter values are calculated during the refinement and found to be  $a = 4.685$  (4) Å,  $b = 3.426$  (4) Å,  $c = 5.133$  (9) Å and  $\beta = 99.356$  which is consistent with literature values (JCPDS Card No. 48–1548,  $a = 4.688$  Å,  $b = 3.422$  Å,  $c = 5.131$  Å and  $\beta = 99.506$ ). The Scherrer formula has been employed to calculate the crystallite size during the refinement, which was found to be ~30 nm.

Surface morphological features of electrospun nanofibers were analyzed by scanning electron microscopy (SEM) and presented in Figure 3. Figure 3a represents the as-spun CuO

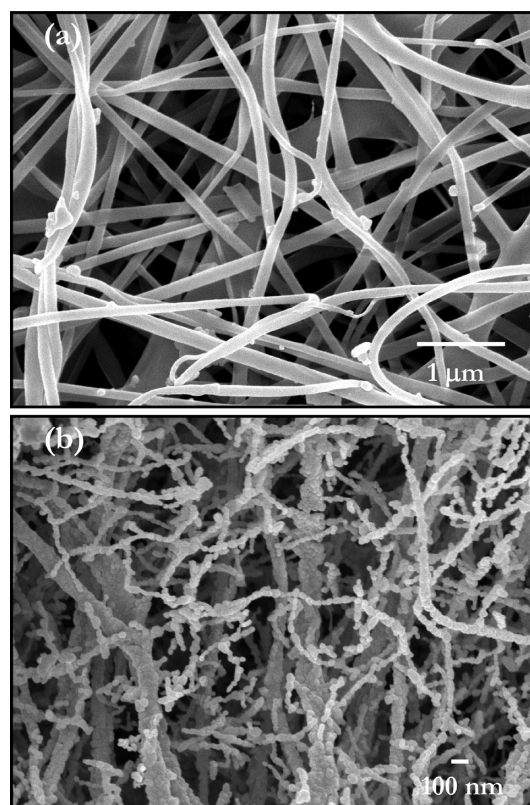


**Figure 3.** Scanning electron microscopic images of (a) as-spun CuO nanofibers and (b) CuO nanofibers sintered at 800 °C for 1 h.

nanofibers with highly interconnected network of fibers comprising of PVA and Cu acetate with large variation in fiber diameters. This randomness of the obtained fiber mesh was the direct consequence of the bending instability associated with the electrospun jet. Reduction of CuO nanofiber diameter upon annealing was observed that is due to the removal of residual polymer in the form of carbon dioxide and water vapor (Figure 3b) and subsequent formation of CuO nanocrystallites along the nanofiber. However, the variation in the fiber diameter was also noted during sintering process. It is observed that the sintered fibers contained nanosized CuO particulates that are interconnected to form a continuous fiber (Figure 3b). Variation in the fiber diameter is mainly ascribed to the different level of nucleation growth that takes place during polymer decomposition and crystallization that simultaneously occur to form a continuous fiber with nanoscopic CuO particles. Aggregation of few nanofiber chains is also noted during high temperature sintering.

Internal crystal structure of the sintered CuO nanofibers were studied by transmission electron microscopy (TEM) and presented in Figure 4. It is evident from the TEM image with different magnifications (Figure 3, parts a and b), that the continuous fibers comprises of nanosized CuO particulates. From the TEM images, the crystal size of CuO particles was found to vary from 20 to 80 nm, whereas the grains were found to be almost in uniform shape. The HR-TEM image of lattice fringes pertaining to CuO nanofibers is illustrated in Figure 4c. The distance between adjacent lattice planes ( $d$ -spacing) were measured and found to be 2.53 Å. This value of  $d$ -spacing was found in good agreement with the ( $h k l$ ) plane ( $-1 1 1$ ) of CuO phase. This indicates that the ( $-1 1 1$ ) plane may predominantly be exposed on the edge of the CuO nanofibers.



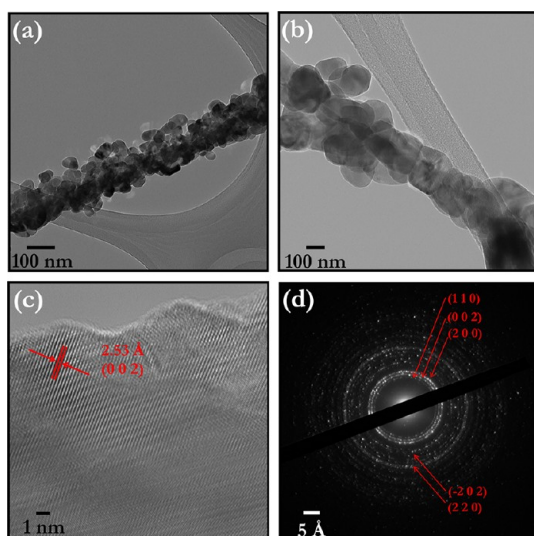


**Figure 4.** Transmission electron microscopic (TEM) pictures of (a and b) CuO nanofibers sintered at 800 °C for 1 h with different magnifications, (c) high-resolution TEM photograph of CuO nanofibers, and (d) selected area electron diffraction pattern.

The selected area electron diffraction (SAED) pattern of CuO nanofibers displays several concentric diffraction rings and some regular diffraction high-lighted spots on the rings (Figure 4d), indicating the well-defined crystalline nature of an assembly of nanofibers which accords well with XRD analysis.

Electrochemical lithium storage properties of CuO-NF was evaluated as anode material for lithium batteries in half-cell configurations and shown in Figure 5. Cyclic voltammetric

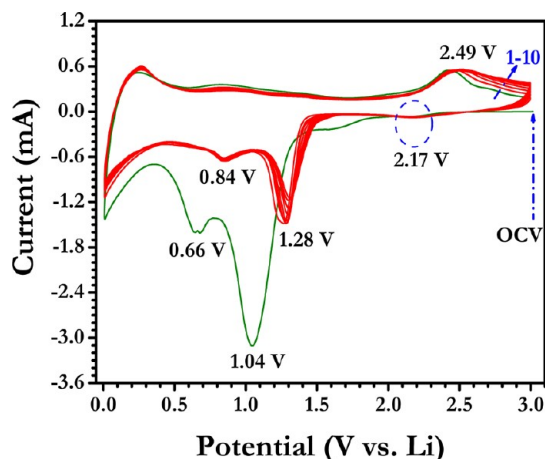


**Figure 5.** Cyclic voltammogram (CV) of Li/CuO nanofiber cell cycled between 0.005 and 3 V vs. Li at scan rate of 0.1 mV s<sup>-1</sup>. In the CV measurements, lithium metal acts as both counter and reference electrode in the two electrode configuration.

(CV) studies of Li/CuO-NF cells were conducted between 0.005–3 V at scan rate of 0.1 mV s<sup>-1</sup>. For the CV measurements metallic lithium acts as both counter and reference electrodes. The test cell, Li/CuO–NF showed the open circuit voltage (OCV) of ~3 V vs Li and first discharged to the lower cutoff potential (5 mV). In the first cathodic sweep the cell showed a weaker broad peak ~2.17 V vs Li which corresponds to the solid solution formation (Li<sub>x</sub>CuO). The sharp peak around ~1.04 V vs Li is associated with the

structural destruction and subsequent formation of Cu<sub>2</sub>O phase.<sup>22</sup> Another reduction reaction takes place at ~0.66 V vs Li and it corresponds to further reduction of Cu<sub>2</sub>O phase in to Cu<sup>0</sup> and amorphous Li<sub>2</sub>O. In addition, partial irreversible electrolyte decomposition also takes place in the latter potential cannot be ruled out. The above two-step process can be described according to the following equilibrium, CuO + 2 Li → Cu<sup>0</sup> + Li<sub>2</sub>O. In the anodic scan, broader oxidation potential ~2.43 V vs Li is attributed to the formation of Cu<sub>2</sub>O (Cu<sup>0</sup> + Li<sub>2</sub>O ↔ Cu<sub>2</sub>O + Li<sub>2</sub>O) and partial oxidation of Cu<sub>2</sub>O in to CuO as well.<sup>35</sup> From the second cycle onward the anodic potentials are shifted toward higher voltages likely ~1.28 and ~0.84 V vs Li. Similarly, the oxidation potential also shifted to ~2.49 V vs Li. In the subsequent cycles, the overlapping of cycling traces (except few initial cycles) is noted during both cathodic and anodic sweeps, which corresponds to the stability of CuO–NF during lithium cycling. Further, area under the peak at ~0.66 V vs Li is comparatively less than at ~1.04 V vs Li which suggests the partial reduction of Cu<sub>2</sub>O phase in to metallic Cu<sup>0</sup> particles. Apart from the morphological features, partial reduction of Cu<sub>2</sub>O phase enables the necessary stability during electrochemical cycling.

Galvanostatic charge–discharge studies were conducted between 0.005 and 3 V vs Li at the constant current density of 100 mA g<sup>-1</sup> and presented in Figure 6. Figure 6a represents

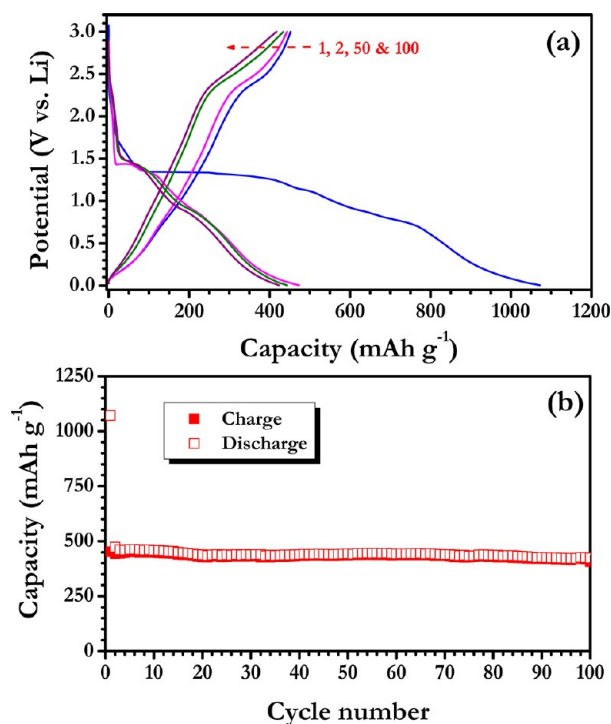


**Figure 6.** (a) Typical galvanostatic charge–discharge curves of Li/CuO nanofiber half-cell cycled between 0.005 and 3 V vs. Li at constant current density of 100 mA g<sup>-1</sup> in room temperature and (b) plot of capacity vs cycle number.

the charge–discharge curves of Li/CuO-NF cell in ambient temperature conditions. The test cell is first discharged and showed the initial discharge capacity of 1071 mAh g<sup>-1</sup>, which is higher than the theoretical capacity of CuO (674 mAh g<sup>-1</sup>) for two electron reaction. In first discharge process, the monotonous slope at ~1.3 V vs Li is ascribed to the lithium insertion into CuO matrix and consequent formation of solid-

solution,  $\text{Li}_x\text{Cu}_{1-x}^{2+}\text{Cu}_x^{+}\text{O}^{22}$ . Approximately,  $\sim 0.15$  mol of lithium ( $\sim 100 \text{ mAh g}^{-1}$ ) per formula unit is intercalated to form intermediate compound  $\text{Li}_{0.15}\text{Cu}_{0.85}^{2+}\text{Cu}_{0.15}^{+}\text{O}$ . Then the predominant structural destruction occurs to form  $\text{Cu}_2\text{O}$  phase exhibiting long distinct plateau around  $\sim 1.34 \text{ V}$  vs Li and further metallic reduction ( $\text{Cu}^0$ ) as well. During the reduction of  $\text{Cu}_2\text{O}$  phase into  $\text{Cu}^0$  metal, the irreversible electrolyte decomposition also noted from the slopping curve. The irreversible decomposition of solution species leads to the formation of solid electrolyte interphase (SEI) and it consumes excess lithium which causes for higher discharge capacity in the first discharge than theoretical limitations. Generally, the irreversible capacity in the first discharge process could originated from the decomposition of electrolyte and consequent formation of SEI layer deposited on the particle surface, which occurs in the low-potential region for transition metal oxides. In the first charge, the reversible capacity of  $452 \text{ mAh g}^{-1}$  is obtained with irreversible capacity of  $619 \text{ mAh g}^{-1}$  in first cycle. After three initial cycles, the coulombic efficiency of Li/CuO-NF cell has been increased to over 98%. The cycling profiles of the Li/CuO-NF cells are illustrated in Figure 6b. It is apparent to notice that, the half-cell exhibited a very stable cycling profile up to 100 cycles tested at constant current density of  $100 \text{ mA g}^{-1}$ . The observed reversible capacity is well over than the theoretical capacity of graphite ( $372 \text{ mAh g}^{-1}$ ). The cell delivered discharge capacity of  $426 \text{ mAh g}^{-1}$  after 100 cycles and the capacity fading is noted  $\sim 0.26 \text{ mAh g}^{-1}$  per cycle with capacity retention of  $\sim 94\%$  after 100 cycles. The improved cycleability is mainly attributed to the unique one-dimensional fibrous morphology composed of nanoscopic CuO particles and partial reduction of  $\text{Cu}_2\text{O}$  phase. A similar kind of improvement in the electrochemical properties were noted for the electrospun  $\text{V}_2\text{O}_5$  nanofibers during Li-insertion/extraction containing fibrous morphology reported earlier.<sup>13</sup> Hence, this clearly indicates that, morphology of the active materials is also very important for the betterment of electrochemical properties. The observed cycling profiles are better than the literature values reported elsewhere (described in Introduction section and Supporting Information) for example, Wan et al.<sup>32</sup> reported the cycleability of pillow shaped CuO and experienced the capacity fade of  $\sim 0.5 \text{ mAh g}^{-1}$  after 50 cycles. Mai et al.<sup>36</sup> reported the CuO/graphene composite with capacity fading of  $\sim 0.65 \text{ mAh g}^{-1}$  after 50 cycles at  $0.1 \text{ C}$  rate (reversible capacity of  $561 \text{ mAh g}^{-1}$ ). As noted from the CV traces, partial reduction of intermediate  $\text{Cu}_2\text{O}$  phase ( $p$  type semiconductor) provides the necessary electronic conductivity during conversion reaction, whereas in other morphologies reported in literature, can able to deliver higher capacity than nanofibers because of complete reduction of  $\text{Cu}_2\text{O}$  in to metallic particles ( $\text{Cu}^0$ ). Further, such partial reduction of  $\text{Cu}_2\text{O}$  phase maintains active materials good contact with current collector by sustaining the unit cell volume variation during the conversion reaction ( $\text{Cu}$  ( $47.24 \text{ \AA}^3$ )  $\leftrightarrow$   $\text{Cu}_2\text{O}$  ( $77.20 \text{ \AA}^3$ )  $\leftrightarrow$   $\text{CuO}$  ( $81.22 \text{ \AA}^3$ )) leads to the enhanced cycleability. The galvanostatic study brings forth the information that, electrospun technique yielded a high performance CuO nanofibers, when employed as anode material for lithium ion batteries compared to the previous reports.<sup>26–31,33,34</sup>

A duplicate cell was assembled to study the electrochemical performances of CuO-NF at high current rates. For the C rate calculation, the reversible capacity  $452 \text{ mAh g}^{-1}$  at current density of  $100 \text{ mA g}^{-1}$  was assumed as  $1 \text{ C}$ . Figure 7 represents the plot of capacity vs cycle number at various current densities.

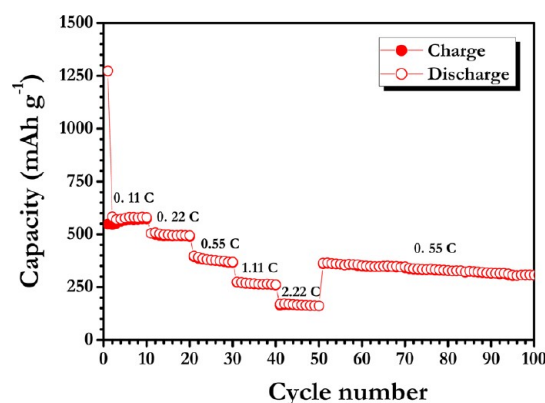


**Figure 7.** Rate capability studies of Li/CuO nanofiber half-cell cycled between 0.005 and 3 V vs. Li at different current rates.

The cell displayed discharge capacities of 580, 498, 394, 274, and  $167 \text{ mAh g}^{-1}$  for 0.11, 0.22, 0.55, 1.11, and  $2.22 \text{ C}$  rates, respectively. It is apparent to notice that, increasing current rate tends to decrease in discharge capacity values. The decrease in capacity values are expected at high current rates, since only surface of the active material participates in the electrochemical reaction owing to kinetic limitations.<sup>37</sup> In other words, in the discharged state containing dominant  $\text{Cu}_2\text{O}$  phase when compared to metallic  $\text{Cu}^0$  particles. The coulombic efficiency of the cell under high current rates is found over 99% except for few initial cycles. The present study clearly demonstrates excellent reversibility of CuO-NF during electrochemical charge–discharge process in half-cell measurements. This result suggests that, electrospun CuO-NF could be used as prospective anode material for lithium-ion batteries. Further studies are in progress to improve the capacity of CuO by tuning various synthesis parameters.

## CONCLUSIONS

CuO nanofibers were synthesized through electrospinning technique and evaluated as anode material for Li-ion battery applications. Phase formation and morphological features were analyzed by X-ray diffraction and SEM, respectively. The CuO nanofibers exhibited relatively high reversible capacity of  $452 \text{ mAh g}^{-1}$  at current density of  $100 \text{ mA g}^{-1}$ . The half-cell Li/CuO nanofibers exhibited excellent cycleability and renders  $\sim 94\%$  of reversible capacity after 100 cycles. We believe that, the morphology played the vital role in the enhancement of cycling profiles. The study provides the possibilities of employing nanostructured transition metal oxides with engineered morphologies preferably patterned by electrospinning techniques as anode materials for lithium-ion batteries. Further studies on the optimization of system/process parameters are in process to fine-tune the electrochemical performance of CuO nanofibers to increasing the reversible capacity.

## ASSOCIATED CONTENT

### Supporting Information

The electrochemical profiles of commercially available CuO particle was compared with present results and illustrated. This material is available free of charge via the Internet at <http://pubs.acs.org>.

## ■ AUTHOR INFORMATION

## Corresponding Author

\*E-mail: seeram@nus.edu.sg (S.R.); Madhavi@ntu.edu.sg (S.M.).

## Author Contributions

<sup>||</sup>Contributed equally

## Notes

The authors declare no competing financial interest.

## ■ ACKNOWLEDGMENTS

This work was supported by a Singapore NRF-CRP grant on "Nanonets for Harnessing Solar Energy and Storage" and also NUS and NTU for providing facilities to carry out the research. V.A. and S.M. wish to thank National Research Foundation, Singapore for the financial support through Clean Energy Research Project (NRF2009EWT-CERP001-036)

## ■ REFERENCES

- (1) Goodenough, J. B.; Kim, Y. *Chem. Mater.* **2009**, *22*, 587–603.
- (2) Aravindan, V.; Gnanaraj, J.; Madhavi, S.; Liu, H.-K. *Chem.—Eur. J.* **2011**, *17*, 14326–14346.
- (3) Song, M.-K.; Park, S.; Alamgir, F. M.; Cho, J.; Liu, M. *Mater. Sci. Eng., Res.* **2011**, *72*, 203–252.
- (4) Etacheri, V.; Marom, R.; Elazari, R.; Salitra, G.; Aurbach, D. *Energy Environ. Sci.* **2011**, *4*, 3243–3262.
- (5) Bruce, P. G.; Scrosati, B.; Tarascon, J.-M. *Angew. Chem., Int. Ed.* **2008**, *47*, 2930–2946.
- (6) Arico, A. S.; Bruce, P.; Scrosati, B.; Tarascon, J.-M.; van Schalkwijk, W. *Nat. Mater.* **2005**, *4*, 366–377.
- (7) Mattevi, C.; Kim, H.; Chhowalla, M. *J. Mater. Chem.* **2011**, *21*, 3324–3334.
- (8) Devaraju, M. K.; Honma, I. *Adv. Energy Mater.* **2012**, *2*, 284–297.
- (9) Aravindan, V.; Karthikeyan, K.; Ravi, S.; Amaresh, S.; Kim, W. S.; Lee, Y. S. *J. Mater. Chem.* **2010**, *20*, 7340–7343.
- (10) Nişancı, F. B.; Demir, Ü. *Langmuir* **2012**, *28*, 8571–8578.
- (11) Cavaliere, S.; Subianto, S.; Savych, I.; Jones, D. J.; Roziere, J. *Energy Environ. Sci.* **2011**, *4*, 4761–4785.
- (12) Zhang, X.; Suresh Kumar, P.; Aravindan, V.; Liu, H. H.; Sundaramurthy, J.; Mhaisalkar, S. G.; Duong, H. M.; Ramakrishna, S.; Madhavi, S. *J. Phys. Chem. C* **2012**, *116*, 14780–14788.
- (13) Cheah, Y. L.; Gupta, N.; Pramana, S. S.; Aravindan, V.; Wee, G.; Srinivasan, M. *J. Power Sources* **2011**, *196*, 6465–6472.
- (14) Cheah, Y. L.; Aravindan, V.; Madhavi, S. *ACS Appl. Mater. Interfaces* **2012**, *4*, 3270–3277.
- (15) Satishkumar, B. C.; Govindaraj, A.; Nath, M.; Rao, C. N. R. *J. Mater. Chem.* **2000**, *10*, 2115–2119.
- (16) Dang, H. Y.; Wang, J.; Fan, S. S. *Nanotechnology* **2003**, *14*, 738.
- (17) Galina, S. Z.; Viktor, L. V.; Victoria, V. I.; Alexander, L. I. *Russ. Chem. Rev.* **2005**, *74*, 587.
- (18) Nishi, Y. *Chem. Rec.* **2001**, *1*, 406–413.
- (19) Park, O. K.; Cho, Y.; Lee, S.; Yoo, H.-C.; Song, H.-K.; Cho, J. *Energy Environ. Sci.* **2011**, *4*, 1621–1633.
- (20) Poizot, P.; Laruelle, S.; Grugeon, S.; Dupont, L.; Tarascon, J. M. *Nature* **2000**, *407*, 496–499.
- (21) Ji, L.; Lin, Z.; Alcoutlabi, M.; Zhang, X. *Energy Environ. Sci.* **2011**, *4*, 2682–2699.
- (22) Debart, A.; Dupont, L.; Poizot, P.; Leriche, J. B.; Tarascon, J. M. *J. Electrochem. Soc.* **2001**, *148*, A1266–A1274.
- (23) Sahay, R.; Sundaramurthy, J.; Suresh Kumar, P.; Thavasi, V.; Mhaisalkar, S. G.; Ramakrishna, S. *J. Solid State Chem.* **2012**, *186*, 261–267.
- (24) Kim, Y.-S.; Hwang, I.-S.; Kim, S.-J.; Lee, C.-Y.; Lee, J.-H. *Sens. Actuators, B* **2008**, *135*, 298–303.
- (25) Wijesundera, R. P. *Semicond. Sci. Technol.* **2010**, *25*, 045015.
- (26) Chen, L. B.; Lu, N.; Xu, C. M.; Yu, H. C.; Wang, T. H. *Electrochim. Acta* **2009**, *54*, 4198–4201.
- (27) Seo, S.-D.; Jin, Y.-H.; Lee, S.-H.; Shim, H.-W.; Kim, D.-W. *Nanoscale Res. Lett.* **2011**, *6*, 397.
- (28) Wang, S. Q.; Zhang, J. Y.; Chen, C. H. *Scr. Mater.* **2007**, *57*, 337–340.
- (29) Huang, X. H.; Wang, C. B.; Zhang, S. Y.; Zhou, F. *Electrochim. Acta* **2011**, *56*, 6752–6756.
- (30) Ju, J.-H.; Ryu, K.-S. *J. Electrochem. Soc.* **2011**, *158*, A814–A817.
- (31) Gao, S.; Yang, S.; Shu, J.; Zhang, S.; Li, Z.; Jiang, K. *J. Phys. Chem. C* **2008**, *112*, 19324–19328.
- (32) Wan, M.; Jin, D.; Feng, R.; Si, L.; Gao, M.; Yue, L. *Inorg. Chem. Commun.* **2011**, *14*, 38–41.
- (33) Wang, F.; Tao, W.; Zhao, M.; Xu, M.; Yang, S.; Sun, Z.; Wang, L.; Song, X. *J. Alloys Compd.* **2011**, *509*, 9798–9803.
- (34) Ke, F.-S.; Huang, L.; Wei, G.-Z.; Xue, L.-J.; Li, J.-T.; Zhang, B.; Chen, S.-R.; Fan, X.-Y.; Sun, S.-G. *Electrochim. Acta* **2009**, *54*, 5825–5829.
- (35) Wang, X.; Tang, D.-M.; Li, H.; Yi, W.; Zhai, T.; Bando, Y.; Golberg, D. *Chem. Commun.* **2012**, 4812–4814.
- (36) Mai, Y. J.; Wang, X. L.; Xiang, J. Y.; Qiao, Y. Q.; Zhang, D.; Gu, C. D.; Tu, J. P. *Electrochim. Acta* **2011**, *56*, 2306–2311.
- (37) Zaghbi, K.; Goodenough, J. B.; Mauger, A.; Julien, C. J. *Power Sources* **2009**, *194*, 1021–1023.